Commun. Comput. Phys.
doi: 10.4208/cicp.110212.021112a

Vol. **14**, No. 3, pp. 599-620
September 2013

Comparison of Fifth-Order WENO Scheme and Finite Volume WENO-Gas-Kinetic Scheme for Inviscid and Viscous Flow Simulation

Jun Luo, Lijun Xuan and Kun Xu*

Mathematics Department, Hong Kong University of Science and Technology, Clear Water Bay, Kowloon, Hong Kong.

Received 11 February 2012; Accepted (in revised version) 2 November 2012

Available online 25 January 2013

Abstract. The development of high-order schemes has been mostly concentrated on the limiters and high-order reconstruction techniques. In this paper, the effect of the flux functions on the performance of high-order schemes will be studied. Based on the same WENO reconstruction, two schemes with different flux functions, i.e., the fifth-order WENO method and the WENO-Gas-kinetic scheme (WENO-GKS), will be compared. The fifth-order finite difference WENO-SW scheme is a characteristic variable reconstruction based method which uses the Steger-Warming flux splitting for inviscid terms, the sixth-order central difference for viscous terms, and three stages Runge-Kutta time stepping for the time integration. On the other hand, the finite volume WENO-GKS is a conservative variable reconstruction based method with the same WENO reconstruction. But, it evaluates a time dependent gas distribution function along a cell interface, and updates the flow variables inside each control volume by integrating the flux function along the boundary of the control volume in both space and time. In order to validate the robustness and accuracy of the schemes, both methods are tested under a wide range of flow conditions: vortex propagation, Mach 3 step problem, and the cavity flow at Reynolds number 3200. Our study shows that both WENO-SW and WENO-GKS yield quantitatively similar results and agree with each other very well provided a sufficient grid resolution is used. With the reduction of mesh points, the WENO-GKS behaves to have less numerical dissipation and present more accurate solutions than those from the WENO-SW in all test cases. For the Navier-Stokes equations, since the WENO-GKS couples inviscid and viscous terms in a single flux evaluation, and the WENO-SW uses an operator splitting technique, it appears that the WENO-SW is more sensitive to the WENO reconstruction and boundary treatment. In terms of efficiency, the finite volume WENO-GKS is about 4 times slower than the finite difference WENO-SW in two dimensional simulations. The current study clearly shows that besides high-order reconstruction, an accurate gas evolution model or flux function in a high-order scheme is also important in the capturing of

*Corresponding author. *Email addresses:* luojun@ust.hk (J. Luo), maljxuan@ust.hk (L. Xuan), makxu@ust.hk (K. Xu)

physical solutions. In a physical flow, the transport, stress deformation, heat conduction, and viscous heating are all coupled in a single gas evolution process. Therefore, it is preferred to develop such a scheme with multi-dimensionality, and unified treatment of inviscid and dissipative terms. A high-order scheme does prefer a high-order gas evolution model. Even with the rapid advances of high-order reconstruction techniques, the first-order dynamics of the Riemann solution becomes the bottleneck for the further development of high-order schemes. In order to avoid the weakness of the low order flux function, the development of high-order schemes relies heavily on the weak solution of the original governing equations for the update of additional degree of freedom, such as the non-conservative gradients of flow variables, which cannot be physically valid in discontinuous regions.

PACS: 02.60Cb, 47.11.Df, 47.45.Ab

Key words: WENO scheme, gas-kinetic scheme, Euler equations, Navier-Stokes equations, high-order methods.

1 Introduction

Computational Fluid Dynamics has made great progress in 1970s and 1980s due to the development of the concept of the nonlinear limiter and the characteristic wave decomposition of the Euler equations. The 2nd-order schemes are mostly used in practical engineering applications at current stage. On the other hand, with the increasing of computational power and the requirement of accurate solutions for more challenging problems, such as compressible turbulent flow and aero-acoustics, the development of reliable high-order methods has attracted much attention [4]. A direct extension of the concept of nonlinear limiter to high-order is the reconstruction schemes of essentially non-oscillatory (ENO) and weighted essentially non-oscillatory (WENO) methods [7,10,14,17]. There are two versions of WENO schemes: finite difference and finite volume. For the rectangular mesh, the main advantage of the finite difference framework is that multi-dimensional calculations do not increase the complexity of the algorithm and the computational cost is much lower than the finite volume version. As tested, a finite volume WENO scheme is usually 4 times more expensive in 2D than a finite difference WENO method due to many flux calculations at the Gaussian points of a cell interface. Therefore, in simple geometry cases, the finite difference WENO scheme is the top choice. The most widely used WENO scheme is the fifth order WENO method [10]. In comparison with other high-order methods, such as discontinuous Galerkin method (DG), the WENO scheme is much more robust and reliable.

The main steps of finite difference WENO scheme are the WENO reconstruction for the fluxes at the cell interface and the Runge-Kutta time stepping to update the flow variables. In the WENO reconstruction, a stencil-weighted technique is used to avoid cross-shock interpolation so as to reduce spurious oscillations. Instead of choosing the smoothest stencil out of many candidates to get the rth order accuracy in the ENO reconstruction, the WENO uses a convex combination of all candidates by assigning a

smoothness-dependent weight to each stencil and results in a $(2r-1)th$ order accuracy. The WENO reconstruction is more accurate, efficient and stable than the ENO reconstruction.

So far, the WENO schemes have found wide applications. The general impression is that the WENO scheme is not sensitive to the fluxes used, such as Lax-Friedrichs or Steger-Warming. The full accuracy of the scheme mainly depends on the order of the reconstruction. One of the purpose of the current paper is to test the effect of flux functions on the performance of high-order schemes. It turns out that besides the high-order initial reconstruction the flux modeling also plays an essential role to capture accurate flow evolution, and to reduce the sensitive dependence of the solution on the initial reconstruction, especially in a barely resolved flow region. All flux functions are equivalent in a well-resolved flow region, because the flux consistency plays a dominant role here. But their performance may deviate from each other in not well-resolved cases, such as 3 or 4 points inside a boundary layer. Currently, in order to increase the accuracy of the WENO scheme, many attempts have been tried to develop hybrid schemes, where the WENO is used in the discontinuous region and high-order compact scheme is used in the smooth region [13, 18]. The aim of the hybrid scheme is to basically develop a method which could make a smooth transition between the upwind and central difference method, because the fundamental basis of the 1st-order Riemann solver for wave decomposition and the flux splitting technique contradicts with the flow physics in the smooth region, where the high-order spatial and temporal evolution are fully coupled. In the smooth region, the traditional central difference approximation with Cauchy-Kowalevskaya technique is far more appropriate to describe flow evolution than upwind concept. The Riemann solution is a low order dynamic model, which is needed to model discontinuous flow in order to introduce enough dissipation. And this amount of dissipation is closely related to the initial jump at the cell interface [26]. Without modifying the 1st-order Riemann dynamic model, the development of high-order schemes becomes a game of reconstruction, since the interface jump is the only freedom many high-order schemes are able to control. Unfortunately, there is no principle to design such an optimal and universal interface jump, and this kind of research will be endless. In order to get out of this dilemma, the use of a high-order dynamic evolution model, which could make a smooth transition between the upwind and central difference scheme, is necessary. For a second order scheme for the inviscid flow, we have such a high-order dynamic model, which is the generalized Riemann solver and the gas-kinetic scheme [1, 11].

In the past decades, a gas-kinetic scheme (GKS) based on the kinetic equation has been developed for the modeling of gas evolution process starting from a discontinuity [12, 16, 26]. Theoretically, the GKS does not target to solve accurately the gas kinetic BGK model [2], but uses the kinetic equation to do the modeling around a cell interface. In the GKS evolution, the whole process from particle free transport to the Navier-Stokes (NS) or Euler solution formation has been recovered [9, 28]. The flow regime of the gas evolution depends on the ratio of time step to the particle collision time. In the smooth flow region, based on the Chapman-Enskog expansion, a time dependent gas distribu-

tion function corresponding to the NS or Euler solutions can be obtained accurately by the GKS. This limiting formulation is basically the central difference method. In the discontinuity region, where the physical solution cannot be well resolved by the numerical cell size, theoretically it is not necessary to know the precise "macroscopic" governing equations here, because it is not needed to incorporate a precise amount of numerical dissipation. But, in such a region the gas evolution model should follow a path which is consistent with the physical one, such as keeping a non-equilibrium gas distribution function at a cell interface to cope with the dissipative mechanism of a physical shock layer [11, 29]. This limiting case is the flux vector splitting upwind method. The advantage of the GKS is that the flux function makes a smooth transition from a upwind (kinetic scale) to a central difference (hydrodynamic scale) method.

Recently, based on the WENO reconstruction and high-order gas-kinetic solution [12], a finite volume high-order WENO-gas-kinetic scheme (WENO-GKS) has been designed and tested for multi-dimensional flows [15]. Different from the traditional WENO scheme, the WENO technique is only used in the data reconstruction of the conservative flow variables at the beginning of each time step. Starting from the high-order reconstruction, a space and time dependent gas distribution function is obtained along the tangential direction of a cell interface, from which the numerical flux is evaluated and used in a finite volume scheme. In GKS, there is no need to use the Runge-Kutta time stepping and Gaussian point integration along a cell interface for the update of flow variables inside each control volume.

Among all WENO schemes we tested, the finite difference WENO method with Steger-Warming flux splitting gives the best results. The detailed formulation of this WENO scheme is presented in Section 3. In order to show the effect of a flux function on the performance of high-order schemes, the numerical solutions of the finite difference WENO-Steger-Warming scheme (WENO-SW) will be compared with that of the finite volume WENO-GKS. The test cases are carefully chosen in order to test the accuracy, the shock-capturing ability, the robustness, and the stability of the schemes. In order to eliminate the numerical error due to the complicated geometry, all tests are conducted in rectangular meshes. The 5th-order WENO reconstruction is used on the characteristic variables in the WENO-SW, and the same WENO reconstruction is used on the conservative variables in the WENO-GKS. The reason we use conservative variables for the WENO-GKS is that the scheme is not sensitive to the variable used in the reconstruction, because the evolution of the whole reconstructed curves will be followed dynamically in the flux evaluation.

2 The 5th order WENO reconstruction

The 5th order WENO reconstruction on a uniform rectangular mesh is a standard reconstruction method [20].

Assume that Q is the variable to be reconstructed. $\bar{Q}_i$ is the cell averaged value in

the *ith* cell. Q_i^l and Q_i^r are the two pointwise values reconstructed at the left and right interfaces of the *ith* cell. The 5th WENO reconstruction is defined as,

$$Q_i^r=\sum_{s=0}^{2} w_s q_i^{(s)}, \qquad Q_i^l=\sum_{s=0}^{2} \tilde{w}_s \tilde{q}_i^{(s)},$$

where

$$q_i^{(0)}=\frac{1}{3}\bar{Q}_i+\frac{5}{6}\bar{Q}_{i+1}-\frac{1}{6}\bar{Q}_{i+2},\quad q_i^{(1)}=-\frac{1}{6}\bar{Q}_{i-1}+\frac{5}{6}\bar{Q}_i+\frac{1}{3}\bar{Q}_{i+1},\quad q_i^{(2)}=\frac{1}{3}\bar{Q}_{i-2}-\frac{7}{6}\bar{Q}_{i-1}+\frac{11}{6}\bar{Q}_i,$$

$$\tilde{q}_i^{(0)}=\frac{11}{6}\bar{Q}_i-\frac{7}{6}\bar{Q}_{i+1}+\frac{1}{3}\bar{Q}_{i+2},\quad \tilde{q}_i^{(1)}=\frac{1}{3}\bar{Q}_{i-1}+\frac{5}{6}\bar{Q}_i-\frac{1}{6}\bar{Q}_{i+1},\quad \tilde{q}_i^{(2)}=-\frac{1}{6}\bar{Q}_{i-2}+\frac{5}{6}\bar{Q}_{i-1}+\frac{1}{3}\bar{Q}_i,$$

$$w_s=\frac{\alpha_s}{\sum_{p=0}^{2}\alpha_p},\quad \alpha_s=\frac{d_s}{(\epsilon+\beta_s)^2},\quad \tilde{w}_s=\frac{\tilde{\alpha}_s}{\sum_{p=0}^{2}\tilde{\alpha}_p},\quad \tilde{\alpha}_s=\frac{\tilde{d}_s}{(\epsilon+\beta_s)^2},\quad s=0,1,2,$$

$$\beta_0=\frac{13}{12}(\bar{Q}_i-2\bar{Q}_{i+1}+\bar{Q}_{i+2})^2+\frac{1}{4}(3\bar{Q}_i-4\bar{Q}_{i+1}+\bar{Q}_{i+2})^2,$$

$$\beta_1=\frac{13}{12}(\bar{Q}_{i-1}-2\bar{Q}_i+\bar{Q}_{i+1})^2+\frac{1}{4}(\bar{Q}_{i-1}-\bar{Q}_{i+1})^2,$$

$$\beta_2=\frac{13}{12}(\bar{Q}_{i-2}-2\bar{Q}_{i-1}+\bar{Q}_i)^2+\frac{1}{4}(\bar{Q}_{i-2}-4\bar{Q}_{i-1}+3\bar{Q}_i)^2,$$

$$d_0=\tilde{d}_2=\frac{3}{10},\quad d_1=\tilde{d}_1=\frac{3}{5},\quad d_2=\tilde{d}_0=\frac{1}{10}.$$

In this paper, in order to distinguish the effect of ϵ on the numerical solution, we will use different values of ϵ. In the numerical tests, "EPS1" means $\epsilon=10^{-6}$ and "EPS2" refers to $\epsilon=10^{-2}$.

For the high-order WENO-GKS, the reconstruction is directly applied on the conservative flow variables. The reason is that the reconstruction on the conservative or characteristic variables will not effect the numerical solution much for the WENO-GKS. However, for the WENO-SW, it is preferred to use the characteristic variables for the accuracy and robustness purpose.

Besides the pointwise values at the cell interface, the WENO-GKS needs subcell resolution, or flow distribution inside each control volume in order to get a time-dependent gas distribution function at a cell interface. Based on the point-wise values and the conservation requirement inside each cell, an initial parabola-type flow distributions can be constructed inside each cell [15].

3 Numerical methods

3.1 High-order WENO-gas-kinetic scheme

3.1.1 High-order gas-kinetic scheme

Here, we briefly introduce the construction of the high-order gas-kinetic scheme. For those who are interested in the detailed derivation, please refer to [12] and [15].

The BGK equation in 2-D is

$$f_t+\vec{u}\cdot\nabla f=\frac{g-f}{\tau}, \tag{3.1}$$

where f is the gas distribution function and g is the equilibrium state approached by f, ∇f is the gradient of f with respect to $\vec{x}$, $\vec{x}=(x,y)$, and $\vec{u}=(u,v)$ is the particle velocity. The particle collision time τ is related to the viscosity and heat conduction coefficients, i.e., $\tau=\mu/p$ where μ is the dynamic viscosity coefficient and p is the pressure. The relation between the macroscopic quantities, such as mass density ρ, momentum density $(\rho U,\rho V)$, and energy density ρE, and the distribution function f is

$$W=\iiint \psi f \mathrm{d}u\mathrm{d}v\mathrm{d}\xi, \tag{3.2}$$

where $W=(\rho,\rho U,\rho V,\rho E)^T$, (U,V) is the macroscopic velocity of the fluid,

$$\psi=(\psi_1,\psi_2,\psi_3,\psi_4)^T=\left(1,u,v,\frac{1}{2}(u^2+v^2+\xi^2)\right)^T,$$

$d\xi=d\xi_1 d\xi_2\cdots d\xi_K$, and K is the number of degrees of internal freedom, i.e., $K=(4-2\gamma)/(\gamma-1)$ for 2-D flow and γ is the specific heat ratio. Since the mass, momentum, and energy are conserved during particle collisions, f and g satisfy the conservation constraint,

$$\iiint (g-f)\psi_\alpha \mathrm{d}u\mathrm{d}v\mathrm{d}\xi=0, \qquad \alpha=1,2,3,4, \tag{3.3}$$

at any point in space and time. The integral solution of (3.1) is

$$f(\vec{x},t,\vec{u},\xi)=\frac{1}{\tau}\int_0^t g(\vec{x'},t',\vec{u},\xi)e^{-(t-t')/\tau}dt'+e^{-t/\tau}f_0(\vec{x}-\vec{u}t,\vec{u},\xi), \tag{3.4}$$

where $\vec{x'}=\vec{x}-\vec{u}(t-t')$ is the particle trajectory. The solution f in (3.4) solely depends on the modeling of f_0 and g.

Based on the Chapman-Enskog expansion of BGK equation (3.1), up to the NS order we can get the corresponding NS distribution function. Therefore, based on the initial discontinuous data, at the cell interface $\vec{x}=(0,0)$, the initial NS distribution function f_0 in the integral solution (3.4) is

$$f_0(\vec{x},\vec{u},\xi)=\begin{cases} f_0^l(\vec{x},\vec{u},\xi), & x<0,\\ f_0^r(\vec{x},\vec{u},\xi), & x>0, \end{cases} \tag{3.5}$$

where

$$\begin{aligned} f_0^{l,r}(\vec{x},\vec{u},\xi)=&g_0^{l,r}[1-\tau(a_1^{l,r}u+a_2^{l,r}v+A^{l,r})]\\ &+g_0^{l,r}[a_1^{l,r}-\tau(((a_1^{l,r})^2+d_{11}^{l,r})u+(a_1^{l,r}a_2^{l,r}+d_{12}^{l,r})v+A^{l,r}a_1^{l,r}+b_1^{l,r})]x\\ &+g_0^{l,r}[a_2^{l,r}-\tau((a_1^{l,r}a_2^{l,r}+d_{12}^{l,r})u+((a_2^{l,r})^2+d_{22}^{l,r})v+A^{l,r}a_2^{l,r}+b_2^{l,r})]y\\ &+\frac{1}{2}g_0^{l,r}((a_1^{l,r})^2+d_{11}^{l,r})x^2+\frac{1}{2}g_0^{l,r}((a_2^{l,r})^2+d_{22}^{l,r})y^2+g_0^{l,r}(a_1^{l,r}a_2^{l,r}+d_{12}^{l,r})xy. \end{aligned} \tag{3.6}$$

Here g_0^l and g_0^r are two Maxwellian distribution functions which correspond to the left and right macroscopic variables respectively. For example, g_0^l corresponding to $W^l = (\rho^l,(\rho^l U^l),(\rho^l V^l),(\rho^l E^l))^T$ has the form

$$g_0^l = \rho^l \left(\frac{\lambda^l}{\pi}\right)^{\frac{K+2}{2}} e^{\lambda^l((u-U^l)^2+(v-V^l)^2+\xi^2)}, \tag{3.7}$$

where λ^l equals to $m/2kT^l$, m is the molecular mass, k is the Boltzmann constant, and T^l is the temperature. For the modeling of the local equilibrium distribution function g, we can use the Taylor expansion of the equilibrium state and get

$$\begin{aligned} g(\vec{x},t,\vec{u},\xi) =& \bar{g}+\bar{g}\bar{a}_1 x+\bar{g}\bar{a}_2 y+\bar{g}\bar{A}t+\frac{1}{2}\bar{g}(\bar{a_1}^2+\bar{d_{11}})x^2+\frac{1}{2}\bar{g}(\bar{a_2}^2+\bar{d_{22}})y^2 \\ &+\bar{g}(\bar{a_1}\bar{a_2}+\bar{d_{12}})xy+\frac{1}{2}\bar{g}(\bar{A}^2+\bar{B})t^2+\bar{g}(\bar{A}\bar{a_1}+\bar{b_1})xt+\bar{g}(\bar{A}\bar{a_2}+\bar{b_2})yt, \end{aligned} \tag{3.8}$$

where $\bar{g}$ is the Maxwellian corresponding to the equilibrium macroscopic state $\bar{W} = (\bar{\rho},(\bar{\rho}\bar{U}),(\bar{\rho}\bar{V}),(\bar{\rho}\bar{E}))^T$ on the cell interface. Because of Eq. (3.3), at $(\vec{x},t)=(0,0,0)$ we have

$$\iiint \bar{g}\psi \mathrm{d}u\mathrm{d}v\mathrm{d}\xi = \bar{W} = \iiint_{u>0} f_0^l(0,\vec{u},\xi)\psi \mathrm{d}u\mathrm{d}v\mathrm{d}\xi + \iiint_{u<0} f_0^r(0,\vec{u},\xi)\psi \mathrm{d}u\mathrm{d}v\mathrm{d}\xi. \tag{3.9}$$

After the modeling of f_0 and g, the time (t) and tangential coordinate (y) dependent distribution function along the cell interface is given by the integral solution (3.4).

The two terms of the BGK-NS solver in (3.4) are

$$\begin{aligned} &\frac{1}{\tau}\int_0^t g(-ut',y-vt',t',\vec{u},\xi)e^{-(t-t')/\tau}dt' \\ =& C_1\bar{g}+C_2\bar{g}\bar{a_1}u+C_1\bar{g}\bar{a_2}y+C_2\bar{g}\bar{a_2}v+C_3\bar{g}\bar{A}+\frac{1}{2}C_4\bar{g}(\bar{a_1}^2+\bar{d_{11}})u^2+\frac{1}{2}C_1\bar{g}(\bar{a_2}^2+\bar{d_{22}})y^2 \\ &+C_2\bar{g}(\bar{a_2}^2+\bar{d_{22}})vy+\frac{1}{2}C_4\bar{g}(\bar{a_2}^2+\bar{d_{22}})v^2+C_2\bar{g}(\bar{a_1}\bar{a_2}+\bar{d_{12}})uy+C_4\bar{g}(\bar{a_1}\bar{a_2}+\bar{d_{12}})uv \\ &+\frac{1}{2}C_5\bar{g}(\bar{A}^2+\bar{B})+C_6\bar{g}(\bar{A}\bar{a_1}+\bar{b_1})u+C_3\bar{g}(\bar{A}\bar{a_2}+\bar{b_2})y+C_6\bar{g}(\bar{A}\bar{a_2}+\bar{b_2})v, \end{aligned} \tag{3.10}$$

and

$$e^{-t/\tau}f_0(-ut,y-vt,\vec{u},\xi) = \begin{cases} C_7 f_0^l(-ut,y-vt,\vec{u},\xi), & u>0, \\ C_7 f_0^r(-ut,y-vt,\vec{u},\xi), & u<0, \end{cases} \tag{3.11}$$

where

$$C_1 = 1-e^{-t/\tau_n}, \quad C_2 = (t+\tau)e^{-t/\tau_n}-\tau, \quad C_3 = t-\tau+\tau e^{-t/\tau_n}, \tag{3.12a}$$

$$C_4 = (-t^2-2\tau t)e^{-t/\tau_n}, \quad C_5 = t^2-2\tau t, \quad C_6 = -\tau t(1+e^{-t/\tau_n}), \quad C_7 = e^{-t/\tau_n}. \tag{3.12b}$$

In any numerical simulation, numerical dissipation is necessary in order to cope with the limited cell resolution. In order to add numerical dissipation but not change the flow

property, in (3.12), we distinguish two particle collision times. One is the physical one (τ) which corresponds to the real collision time in the Chapman-Enskog expansion for the Navier-Stokes solution, and another one is the numerical one (τ_n) which takes into account the effect of initial pressure jump at the cell interface. As considered in [15], the BGK-NS solver uses

$$\tau=\mu/\bar{p},\ \ \tau_n=\mu/\bar{p}+\beta\Delta x\sqrt{\bar{\lambda}}|p^l-p^r|/(p^l+p^r), \tag{3.13}$$

where β is a constant parameter, Δx is the cell size, $\bar{p}$ is the pressure corresponding to the equilibrium state $\bar{g}$, $\bar{\lambda}$ is given in the equilibrium state $\bar{g}$, and p^l and p^r are the pressure jump at the cell interface in the initial reconstructed data.

The BGK-Euler solver is a special case when physical collision time $\tau=0$. In BGK-Euler solver, the numerical collision time is defined by

$$\tau_n=\alpha\Delta x\sqrt{\bar{\lambda}}+\beta\Delta x\sqrt{\bar{\lambda}}|p^l-p^r|/(p^l+p^r), \tag{3.14}$$

where α and β are two constants. The reason for the above construction is the following. For the inviscid flow, as mesh size goes to zero, τ_n will go to zero as well. Therefore, the GKS converges to the Euler solutions. For well-resolved flow without initial discontinuities, due to the small value of τ_n the gas will converge to the equilibrium state quickly. However, in the dissipative shock region, the particle collision time will take a much large numerical value so as to capture the non-equilibrium numerical shock thickness, which is on the order of cell size. This dynamics mimics the real physical process inside a shock layer. This is equivalent to enlarging the physical shock thickness to the cell size scale through the additional numerical dissipation by increasing the particle collision time.

The calculation of the coefficients $a_1^l, a_1^r, \bar{a_1}, \cdots, A^l, A^r, \bar{A}, \cdots$ in the distribution functions are related to the high-order slopes of macroscopic variables, which are presented in [15]. The integral solution (3.4) basically describes a gas evolution process from the collision-less (upwind) transport to the equilibrium state evolution (central difference). More specifically, the evolution covers from the kinetic scale (particle mean free path) to the hydrodynamic scale (gradient of macroscopic variables) gas evolution.

3.1.2 Gas-kinetic flow transport

For a finite volume scheme, the fluxes across a cell interface are defined by

$$F=\iiint u\psi f\mathrm{d}u\mathrm{d}v\mathrm{d}\xi, \tag{3.15}$$

where $F=(F_\rho, F_{\rho U}, F_{\rho V}, F_{\rho E})^T$ depend on the gas distribution function f in (3.4) at the cell interface. For a rectangular cell bounded by the straight lines, $x=x_{i-1/2}$, $x=x_{i+1/2}$, $y=y_{j-1/2}$ and $y=y_{j+1/2}$, the update of the cell-average conservative variables W_{ij} inside a control volume $\Delta x\Delta y=(x_{i+1/2}-x_{i-1/2})\times(y_{j+1/2}-y_{j-1/2})$ from time step t_n to t_{n+1}

becomes

$$W_{ij}^{n+1}=W_{ij}^{n}+\frac{1}{\Delta x\Delta y}\int_{t_n}^{t_{n+1}}\int_{-\frac{1}{2}\Delta x_i}^{\frac{1}{2}\Delta x_i}\left[F_{j-1/2}(t,x)-F_{j+1/2}(t,x)\right]dxdt$$
$$+\frac{1}{\Delta x\Delta y}\int_{t_n}^{t_{n+1}}\int_{-\frac{1}{2}\Delta y_j}^{\frac{1}{2}\Delta y_j}\left[F_{i-1/2}(t,y)-F_{i+1/2}(t,y)\right]dydt, \tag{3.16}$$

where $F_{j-1/2}(t,x),F_{j+1/2}(t,x),F_{i-1/2}(t,y),F_{i+1/2}(t,y)$ are the fluxes along the four cell interfaces respectively. Because the time-dependent fluxes can be explicitly integrated along a cell interface in the GKS, the final scheme presents a high-order flow transport through the interface within a time step without using Runge-Kutta time stepping and flux construction at Gauss points.

3.2 WENO-Steger-Warming scheme

The WENO-SW solves the hydrodynamic equations

$$W_t+F(W)_x+G(W)_y=F^v(W,W_x,W_y)_x+G^v(W,W_x,W_y)_y, \tag{3.17}$$

where W is the conservative variables, F and G are the inviscid fluxes, and F^v and G^v are the viscous fluxes. For a finite-difference scheme, we need to construct both inviscid and viscous fluxes at the cell interface.

The following WENO scheme is the 5th order finite-difference WENO-Steger-Warming scheme, where the Steger-Warming splitting [23] is used to obtain the inviscid fluxes at the cell interface.

3.2.1 Inviscid flux reconstruction

The x-direction flux F can be decomposed as

$$F=R\Lambda LW, \tag{3.18}$$

where $\Lambda=diag[\lambda_1,\lambda_2,\cdots,\lambda_n]$ is a diagonal matrix with eigenvalues of $\partial F/\partial W$, R is the right eigenvector matrix and L is the left one, n is the number of the equations. Then, F can be split according to

$$F=F^+ +F^-. \tag{3.19}$$

In the Steger-Warming splitting,

$$F^{\pm}=R\Lambda^{\pm}LW, \quad \Lambda=\Lambda^+ +\Lambda^-. \tag{3.20}$$

and

$$\Lambda^{\pm}=diag[\lambda_1^{\pm},\lambda_2^{\pm},\cdots,\lambda_n^{\pm}] \quad \text{with} \quad \lambda_i^{\pm}=\frac{\lambda_i\pm\sqrt{\lambda_i^2+\varepsilon}}{2} \quad (i=1,\cdots,n), \tag{3.21}$$

where ε is a small constant. In our simulation, $\varepsilon=1.0e-3$.

For the construction of the numerical x-direction flux $\hat{F}_{i+1/2,j}$ at the cell interface $(x_{i+1/2},y_j)$ of the cell (i,j), we use the following steps.

1. Split the fluxes $F_{i+l,j}$ $(l=-2,\cdots,3)$ in the surrounding cells to get $F^{\pm}_{i+l,j}$ $(l=-2,\cdots,3)$.
2. Use the variable $W_{i+1/2,j}=(W_{i,j}+W_{i+1,j})/2$ to calculate the left and right eigenvector matrix $L_{i+1/2,j}$ and $R_{i+1/2,j}$ at the cell interface.
3. Change the conservative fluxes $F^{\pm}_{i+l,j}$ $(l=-2,\cdots,3)$ to the characteristic fluxes $\tilde{F}^{\pm}_{i+l,j}$ $(l=-2,\cdots,3)$ by
$$\tilde{F}^{\pm}_{i+l,j}=L_{i+l/2,j}F^{\pm}_{i+l,j} \quad (l=-2,\cdots,3).$$
4. Use the 5th order WENO reconstruction (see Section 2) on the characteristic fluxes $\tilde{F}^{\pm}_{i+l,j}$ $(l=-2,\cdots,3)$ to get the characteristic flux $\tilde{F}^{\pm}_{i+1/2,j}$, and calculate the final characteristic flux $\tilde{F}_{i+1/2,j}=\tilde{F}^{+}_{i+1/2,j}+\tilde{F}^{-}_{i+1/2,j}$.
5. Construct the fluxes for the conservative variables at the cell interface by
$$\hat{F}_{i+1/2,j}=R_{i+1/2,j}\tilde{F}_{i+1/2,j}.$$

In a similar way, we can get the y-directional numerical flux $\hat{G}_{i,j+1/2}$ at the cell interface $(x_i,y_{j+1/2})$.

3.2.2 Viscous flux reconstruction

The viscous fluxes F^v and G^v are related to the derivatives of flow variables. For the NS equations, we need to calculate T_x, U_x, U_y, V_x and V_y in order to get the x-direction viscous flux F^v, where T is the temperature, U is the x-direction velocity, and V is the y-direction velocity. So, the basic step is to construct the derivatives of a variable q.

Firstly, in each cell (i,j), we use a 6^{th}-order central difference to calculate the derivative, i.e.,
$$\left(\frac{\partial q}{\partial x}\right)_{i,j}=\frac{45(q_{i+1,j}+q_{i-1,j})-9(q_{i+2,j}-q_{i-2,j})+q_{i+3,j}-q_{i-3,j}}{60\Delta x}. \tag{3.22}$$
Then, with all the derivatives, we can calculate the x-directional and y-directional viscous fluxes $F^v_{i,j}$ and $G^v_{i,j}$ in each cell. Finally, the numerical viscous fluxes at the cell interfaces can be calculated by the 6th order central interpolation
$$\hat{F}^v_{i+1/2,j}=\frac{37(F^v_{i,j}+F^v_{i+1,j})-8(F^v_{i-1,j}+F^v_{i+2,j})+F^v_{i-2,j}+F^v_{i+3,j}}{60}, \tag{3.23a}$$
$$\hat{G}^v_{i,j+1/2}=\frac{37(G^v_{i,j}+G^v_{i,j+1})-8(G^v_{i,j-1}+G^v_{i,j+2})+G^v_{i,j-2}+G^v_{i,j+3}}{60}. \tag{3.23b}$$

3.2.3 Time evolution

The final numerical fluxes at the cell interface are denoted by
$$\hat{\mathcal{F}}_{i+1/2,j}=\hat{F}_{i+1/2,j}-\hat{F}^v_{i+1/2,j}, \tag{3.24a}$$
$$\hat{\mathcal{G}}_{i,j+1/2}=\hat{G}_{i,j+1/2}-\hat{G}^v_{i,j+1/2}. \tag{3.24b}$$

With the above numerical fluxes, we can get the increment

$$\Delta W_{i,j}=\frac{\hat{\mathcal{F}}_{i+1/2,j}-\hat{\mathcal{F}}_{i-1/2,j}}{\Delta x}+\frac{\hat{\mathcal{G}}_{i,j+1/2}-\hat{\mathcal{G}}_{i,j-1/2}}{\Delta y}. \tag{3.25}$$

A 3^{rd}-order TVD Runge-Kutta method is used to finish the time evolution,

$$W_{i,j}^{(1)}=W_{i,j}^{n}-\Delta t\Delta W_{i,j}(W^{n}), \tag{3.26a}$$

$$W_{i,j}^{(2)}=\frac{3}{4}W_{i,j}^{n}+\frac{1}{4}[W_{i,j}^{(1)}-\Delta t\Delta W_{i,j}(W^{(1)})], \tag{3.26b}$$

$$W_{i,j}^{(n+1)}=\frac{1}{3}W_{i,j}^{n}+\frac{2}{3}[W_{i,j}^{(2)}-\Delta t\Delta W_{i,j}(W^{(2)})]. \tag{3.26c}$$

4 Numerical examples

For all tests in this paper, the time step is determined by the CFL condition with CFL number 0.5.

4.1 Mach 3 step problem

The Mach 3 step problem was first proposed by Woodward and Colella in [25]. The computational domain is $[0,3]\times[0,1]$. A step with height 0.2 is located at x=0.6. The upstream velocity is $(U,V)=(3,0)$. The adiabatic slip Euler boundary condition is implemented at all boundaries.

As explained in [25], the corner of the step is the center of a rarefaction fan and it is a singular point of the flow. The flow will be much affected by the numerical errors generated just in the neighborhood of this singular point. Almost for all WENO schemes, in order to get better results, a special treatment introduced in [25] has been applied. Or, a refined mesh is used around the corner. In order to avoid confusion and compare the results of the WENO-GKS and the WENO-SW truthfully, there is no special treatment anywhere in the current study. The parameter $\epsilon=10^{-6}$ in the 5th order WENO reconstruction is used. In the WENO-GKS, $\alpha=0$ and $\beta=100$ for numerical collision time in (3.14).

Figs. 1, 2 and 3 present the numerical solutions from both WENO-SW and WENO-GKS with different number of mesh points, i.e., $120\times40, 60\times20$, and 30×10. All these results are consistent with the flow structures in [25]. Based on the these figures, the WENO-SW gives a large tilted Mach stem above the up surface of the step, and the WENO-GKS presents a much straighter and shorter one. After a few shock reflections, the shock front of the WENO-SW gets smeared and disappeared in the case with 30×10 mesh points case. But, for the WENO-GKS, the shock reflection can be observed clearly in the coarse mesh case. This illustrates that WENO-SW has large numerical dissipation in comparison with WENO-GKS. In order to understand why the WENO-SW has a tilted

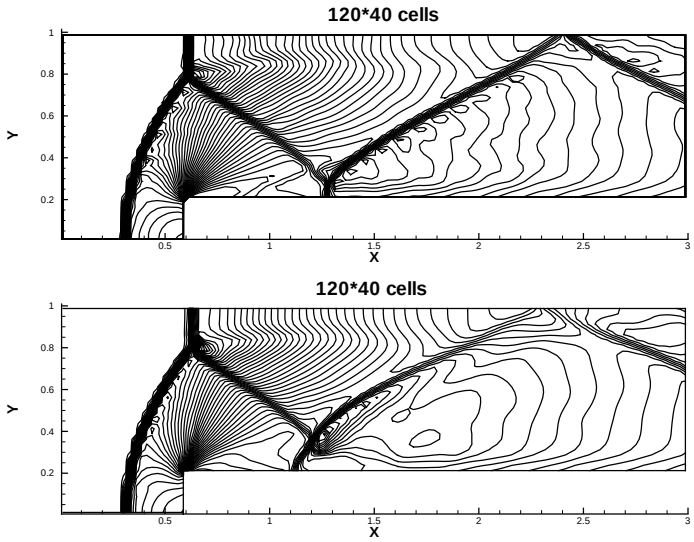

Figure 1: Mach 3 step problem: density distribution at $t=4.0$ with 120×40 mesh points by the WENO-GKS (upper one) and the WENO-SW (lower one). In each figure, there are 50 contours from 0.5 to 5.

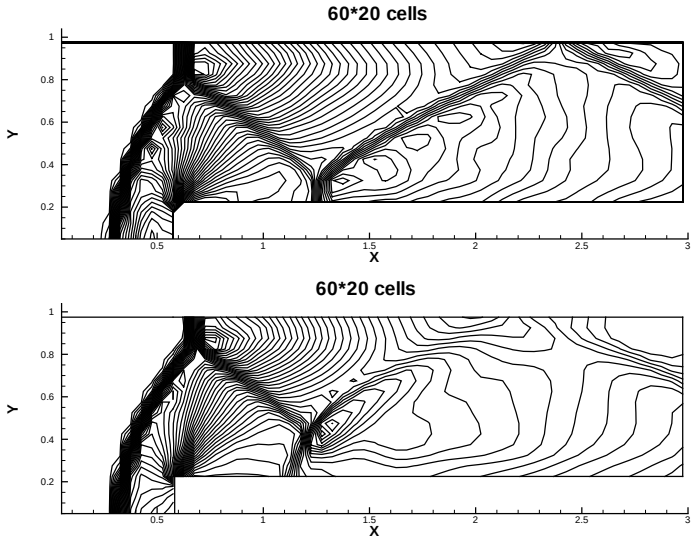

Figure 2: Mach 3 step problem: density distribution at $t=4.0$ with 60×20 mesh points by the WENO-GKS (upper one) and the WENO-SW (lower one). In each figure, there are 50 contours from 0.5 to 5.

Mach stem, the WENO-GKS is tested for the NS solution with Reynolds number 1000, but with the Euler boundary condition. Fig. 4 shows the comparison of WENO-SW for the inviscid flow and WENO-GKS for the viscous flow. It shows that the solution given by the WENO-SW is more close to a viscous solution. This indicates again that a high level of numerical dissipation exists in the WENO-SW.

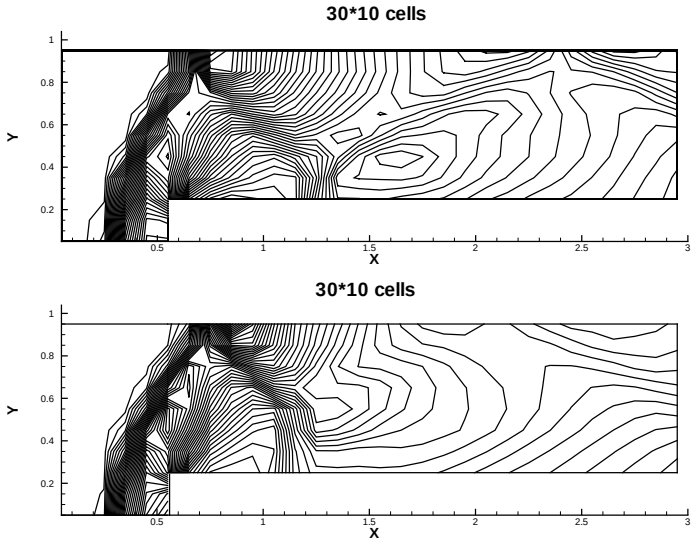

Figure 3: Mach 3 step problem: density distribution at $t=4.0$ with 30×10 mesh points by the WENO-GKS (upper one) and the WENO-SW (lower one). In each figure, there are 50 contours from 0.5 to 5.

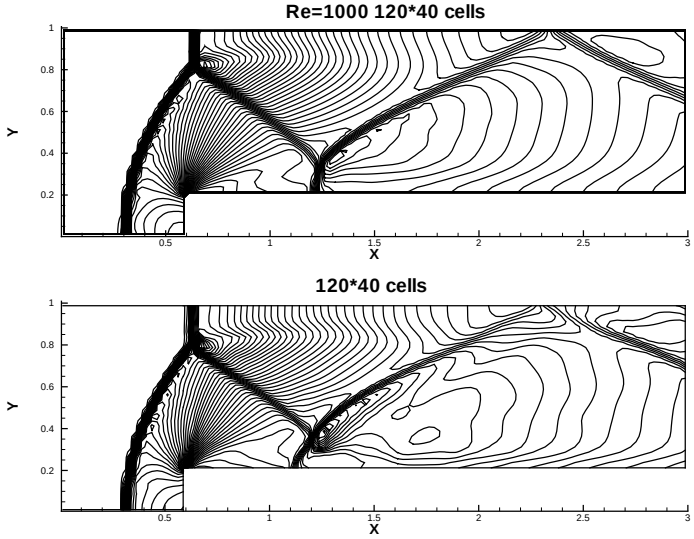

Figure 4: Mach 3 step problem: density distribution at $t=4.0$ with 120×40 mesh points. Upper one: NS solution with Reynolds number 1000 by the WENO-GKS. Lower one: Euler solution by the WENO-SW. In each figure, there are 50 contours from 0.5 to 5.

4.2 Isentropic periodic vortex propagation

This is a test for the accuracy of the Euler solutions (see [13, 20]). The initial condition is given by

$$(U(x,x,0),V(x,y,0))=(1,1)+\frac{\kappa}{2\pi}e^{0.5(1-r^2)}(-\bar{y},\bar{x}),$$

$$T(x,y,0)=1-\frac{(\gamma-1)\kappa^2}{8\gamma\pi^2}e^{1-r^2},\qquad S(x,y,0)=1,$$

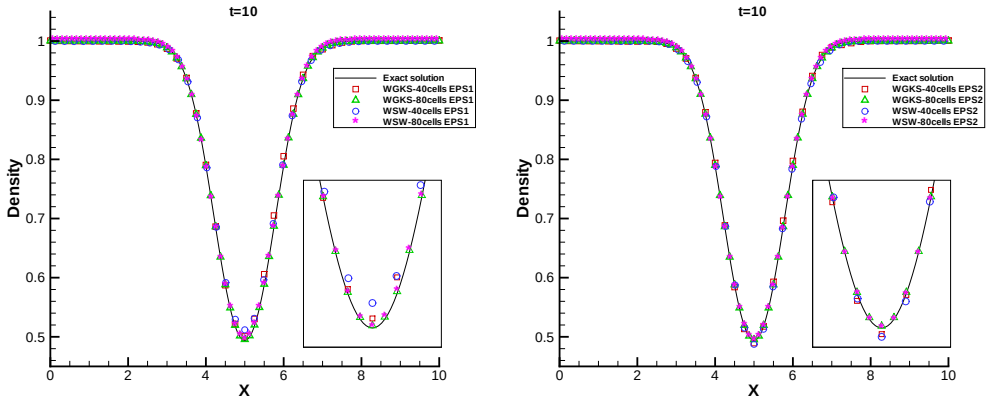

Figure 5: Isentropic periodic vortex propagation: density distribution at $t=10$ (1 period) by the WENO-GKS (WGKS) and the WENO-SW (WSW).

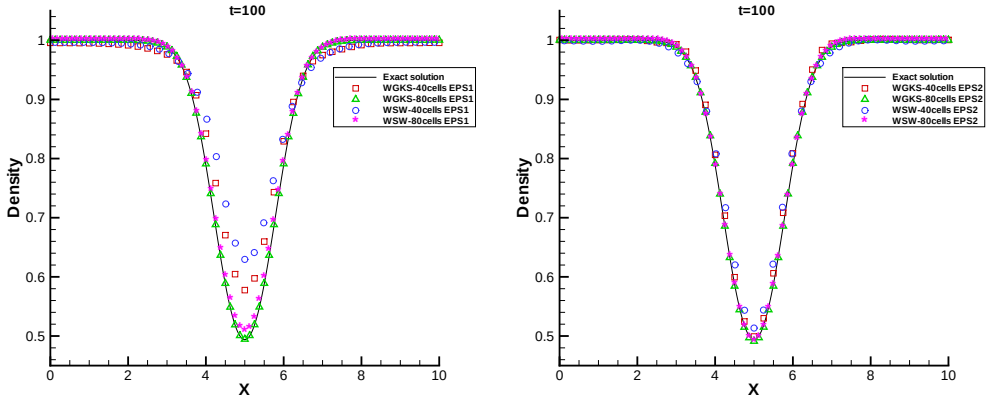

Figure 6: Isentropic periodic vortex propagation: density distribution at $t=100$ (10 periods) by the WENO-GKS (WGKS) and the WENO-SW (WSW).

where the temperature T and the entropy S are related to the density ρ and the pressure p by

$$T=\frac{p}{\rho}, \qquad S=\frac{p}{\rho^{\gamma}},$$

and $(\bar{x},\bar{y})=(x-5,y-5)$, $r^2=\bar{x}^2+\bar{y}^2$, and the vortex strength $\kappa=5$. The computational domain is $[0,10]\times[0,10]$. The periodic boundary condition is used in both directions.

The numerical results with 80×80 and 40×40 cells at $t=10$ (1 period) and $t=100$ (10 periods) are shown in Figs. 5 and 6 for both WENO-SW and WENO-GKS. In order to show the relationship between the parameter ϵ in the WENO reconstruction and the accuracy of the numerical solution, we test this case with two different ϵ, which are EPS1 ($\epsilon=10^{-6}$) and EPS2 ($\epsilon=10^{-2}$). Theoretically, a large value of ϵ presents a reconstruction with more equally weights for different stencils. For a smooth flow, a small ϵ makes the

reconstruction to reduce to a 3rd order interpretation. A larger ϵ balances the weights of different stencils and make the reconstruction to be close to the 5th order interpolation. As shown in Figs. 5 and 6, for such a smooth flow, in general, the reconstruction with EPS2 will give more accurate and less dissipative results than that from EPS1 for both WENO-SW and WENO-GKS. At the same time, for both meshes the results from WENO-GKS are more accurate than these from WENO-SW, especially at a mesh size 40×40 and $t=100$, see Fig. 6. At time $t=10$ and 40×40 mesh points, see Fig. 5, EPS1 introduces numerical dissipation and presents undershoot for both WENO-SW and WENO-GKS. However, with EPS2, the WENO reconstruction introduces overshoot for both schemes. But, in both cases due to the time accurate gas evolution model in the gas-kinetic scheme, the WENO-GKS could increase the undershoot and decrease the overshoot in comparison with WENO-SW. In other words, the WENO-GKS has a better capacity to drive the solution in the correct direction due to the participation of the subcell flow distribution in the construction of the dynamical flux function. More specifically, the gas-kinetic flux function does not only depend on the flow variables at the cell interface, but also takes into account the whole curve evolution around the interface.

Based on the above test, we can clearly realize that even though the gas-kinetic scheme is not solving the inviscid Euler equations directly, it gives accurate inviscid solution. In general, the numerical dissipation of the gas-kinetic scheme is less than the schemes based on the Riemann solvers, since the GKS can make a smooth transition from the upwind to the central difference. This is one of the reason for the reduction of numerical dissipation in GKS in the smooth flow region.

4.3 Cavity flow

The cavity flow at low Mach number is a standard test case for validating incompressible or low speed NS flow solvers. This is also a good test case for the shock capturing scheme in validating its capacity in capturing the Navier-Stokes solutions, especially with the non-linear limiters involved. For a directional splitting finite volume scheme, it will be difficult to present an accurate viscous solution with strong vortex structure. Fortunately, the finite difference WENO-SW is an intrinsic multi-dimensional scheme due to its simultaneous evaluation of ∂x and ∂y terms of the NS equations at a grid point. At the same time, the finite volume WENO-GKS has a multi-dimensional flux function as well, where both x- and y-direction flow derivatives contributes to the flux in the interface normal direction.

The flow is bounded by a unit square and is driven by a uniform translation of the top boundary. In the simulation, the diatomic gas $\gamma=1.4$ is considered. The boundary is isothermal and nonslip, and the flow condition is $Ma=0.3$ and $Re=3200$, where Ma is the Mach number and Re is the Reynolds number. Since the benchmark solution is from incompressible NS equations, in order to avoid kinematic dissipation [6, 27], most simulations in the past are based on the numerical methods for the incompressible equations or the artificial compressibility ones, where a continuous initial reconstruction across a

cell interface is assumed. However, here we are going to use the same shock capturing WENO reconstruction in the cavity simulation. This is challenge for any shock capturing NS flow solver, because the cell interface discontinuity may generate large numerical dissipation.

In order to get the best results for the WENO-SW, we tested many boundary condition treatments and finally choose the following reconstruction. The special treatment is the following. The temperature and velocities are given directly since the boundary is isothermal and nonslip. Other data at the boundary are extrapolated from the flow. For the WENO-SW, the three layer interfaces close to the cavity wall but inside the computational domain are specially treated. For the first layer cell interface, a $3rd$-order extrapolation is used to reconstruct the conservative variable fluxes. For the second interface, a $4th$-order interpolation is used to reconstruct the conservative variable fluxes. For the third interface, a $5th$-order upwind interpolation is used to reconstruct the characteristic fluxes. We use a $4th$-order interpolation to reconstruct the viscous fluxes at all of the three interfaces. For the WENO-GKS, the boundary treatment is relatively simple. A $5th$-order extrapolation for the conservative variables is used at the boundary.

Firstly, we compare the efficiency in the cavity simulation for both schemes. The results are shown in Table 1. As shown in the table, the WENO-GKS is about 4 times slower than the WENO-SW. This shows that the speed of WENO-GKS is similar to a finite volume WENO scheme. As shown in [21], the computational cost of the finite volume WENO scheme is indeed at least 4 times more expensive than the finite difference one in a two-dimensional simulation.

Table 1: Average computational time for one time-step.

CPU time (seconds)	WENO-GKS	WENO-SW
33×33 cells	1.8776e-002	4.3276e-003
65×65 cells	7.4369e-002	1.6433e-002

For the cavity flow simulations, we use three sets of meshes, which are 101×101, 65×65, and 33×33 for both schemes. Fig. 7 shows the distributions of streamline for both schemes with a mesh of 65×65 points. Except around the up left corner, the streamlines from both WENO-SW and WENO-GKS are close to each other.

The results of U-velocity along the vertical symmetric line at $x=0.5$ and V-velocity along the horizontal symmetric line at $y=0.5$ with different mesh sizes will be presented in detail. Fig. 8 shows U and V velocity distributions for a mesh with 101×101 points. The benchmark solution is from [5, 24]. As shown in this figure, the results from both WENO-SW and WENO-GKS are consistent with the reference solutions. The reconstruction with EPS1 presenting a better shock capturing property turns out to be more dissipative than those with EPS2. This is clearly observed in the V-velocity for the WENO-SW. The WENO-GKS solutions are less sensitive to the values of ϵ. At such a refined mesh, it is hard to distinguish the two solutions from WENO-GKS. The overall solutions from WENO-GKS are closer to the benchmark ones than the WENO-SW results.

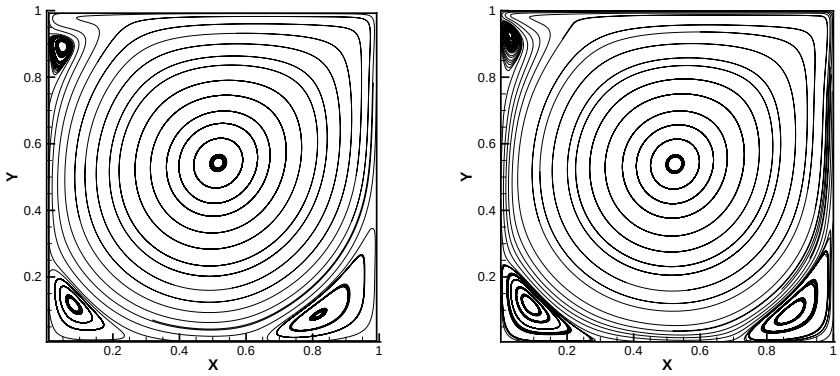

Figure 7: Cavity flow ($Re=3200$, $Ma=0.3$): streamlines with 65×65 mesh points. The left one: streamline by the WENO-GKS. The right one: streamline by the WENO-SW.

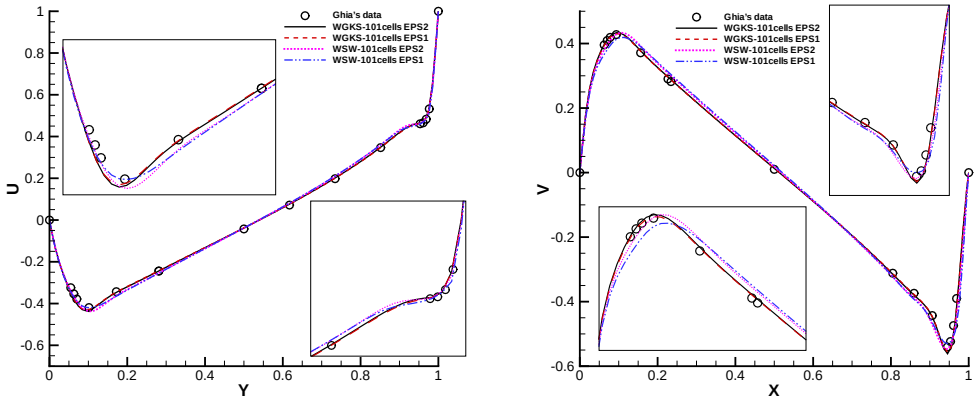

Figure 8: Cavity flow at $Re=3200$ and $Ma=0.3$ with 101×101 mesh points. U-velocity along the vertical symmetric line at $x=0.5$ (upper figure) and V-velocity along the horizontal symmetric line at $y=0.5$ (lower figure) by the WENO-GKS(WGKS) and the WENO-SW(WSW). The benchmark solution is from [5].

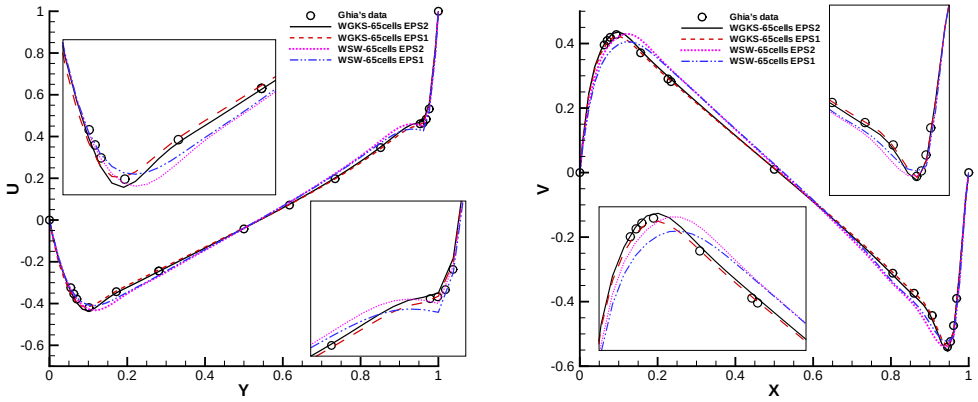

Figure 9: Cavity flow at $Re=3200$ and $Ma=0.3$ with 65×65 mesh points. U-velocity along the vertical symmetric line at $x=0.5$ (upper figure) and V-velocity along the horizontal symmetric line at $y=0.5$ (lower figure) by the WENO-GKS (WGKS) and the WENO-SW (WSW). The benchmark solution is from [5].

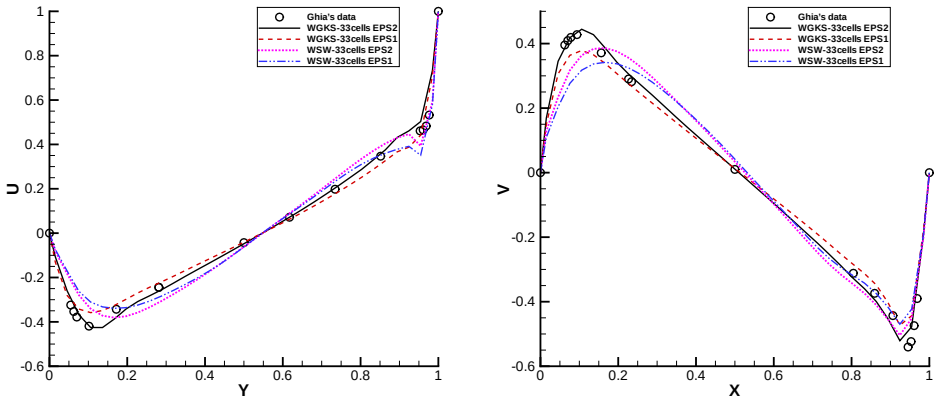

Figure 10: Cavity flow at $Re=3200$ and $Ma=0.3$ with 33×33 mesh points. U-velocity along the vertical symmetric line at $x=0.5$ (upper figure) and V-velocity along the horizontal symmetric line at $y=0.5$ (lower figure) by the WENO-GKS (WGKS) and the WENO-SW (WSW). The benchmark solution is from [5].

As the mesh points reduce to 65×65, the results from both scheme are shown in Fig. 9. As seen in this figure, the distinction between the results from different schemes and different ϵ becomes much clear. Same as Fig. 8, the schemes with EPS1 present more dissipative results than that using EPS2. Both results from WENO-SW with EPS1 and EPS2 are worse than the corresponding ones from WENO-GKS. This figure confirms the previous conclusion that the WENO-GKS has less numerical dissipation than WENO-SW. The WENO-SW is more sensitive to the WENO reconstruction.

Fig. 10 shows the results with a mesh of 33×33 points. Even though the solution from WENO-SW deteriorates quickly, the general conclusion is the same as that from the previous figures. It is surprising that with EPS2, even with such a coarse mesh the WENO-GKS can present very accurate solution. A small ϵ increases the shock capturing capacity, but does introduce more numerical dissipation, such as reducing the peak V velocity around the left boundary for both schemes. However, with such a coarse mesh, the boundary layer thickness of WENO-GKS is still correct. The solutions inside the cavity can be kept much better by the WENO-GKS.

Theoretically, the cavity flow should reach a steady-state solution, where the solution differences at time $(t-\delta t)$ and t should become smaller and smaller as t increases, and δt is a fixed time interval. Hence, we can check the time-convergence rate of a scheme in this case. Fig. 11 shows the error defined by

$$\text{Error}(t)=\frac{\sum_{i,j}|\rho(x_i,y_j,t)-\rho(x_i,y_j,t-10)|}{\mathcal{N}},$$

where ρ is the density, $\mathcal{N}$ is the total number of mesh points. For the WENO-GKS, the error decreases continuously in the case with 65×65 mesh points. But, it keeps a constant value around 10^{-6} in the case with 33×33 mesh points. The WENO-SW has a much larger error than WENO-GKS. With a mesh size 65×65, the error from WENO-SW keeps increasing with time. The main reason for the good performance of gas kinetic scheme

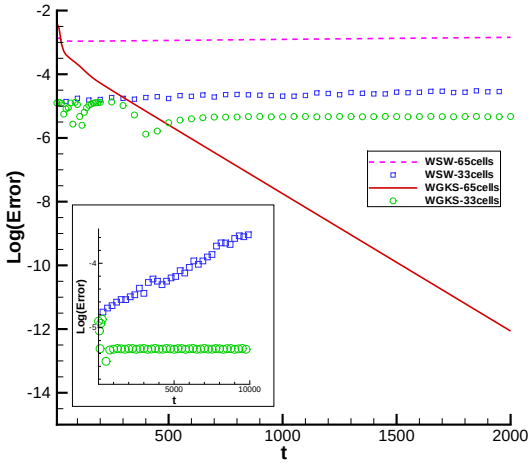

Figure 11: Cavity flow at $Re=3200$ and $Ma=0.3$. The convergence history of the numerical solution with mesh sizes 65×65 and 33×33 by the WENO-SW (WSW) and the WENO-GKS (WGKS) schemes.

is that it gives a NS solution directly from a single initial reconstruction without splitting the inviscid and viscous terms. For the WENO-SW, the two flux construction are based on two different initial flow condition. At a refined mesh, the initial data for the construction of inviscid and viscous terms in the WENO-SW are close to each other, and the results become acceptable. However, as the mesh points are reduced, the initial data for the inviscid and viscous terms will deviate away each other for the WENO-SW due to their different construction. As a result, the inconsistency in the evolution model from two different initial data prevents the WENO-SW from converging. To keep a consistent discretization for the inviscid and viscous terms of the NS equations is a challenge problem for any high-order scheme, especially in the regions where the flow structure can be barely resolved. This problem will persist because in a practical flow simulation not all flow structures can be well-resolved, such as the turbulence. Therefore, much attention should be paid to develop un-splitting high-order methods for the NS equations.

The cavity case clearly demonstrates the superiority of the WENO-GKS over the WENO-SW. Even though it is more expensive, the WENO-GKS is much more accurate and robust. Certainly, there are many 5th WENO schemes. The scheme we tested here may not be an optimal one. In order to reduce a systematic error due to biased selection of WENO schemes, we also tried the WENO methods in [8, 19]. The WENO-SW solutions presented in the current paper are more accurate than those WENO solutions in the literature. In [8, 19], the cavity solutions from other WENO schemes are presented.

5 Conclusion

In this paper, two high-order WENO-type schemes are tested in a few cases from smooth vortex propagation to the strong shock interactions. The schemes compared are the fi-

nite difference WENO-Steger-Warming scheme and the finite volume WENO-gas-kinetic scheme. Since the main purpose of this comparison is to figure out the importance of a flux function on the accuracy, robustness, and the stability of a numerical method, both schemes are based on the same 5th-WENO reconstruction. Any difference is solely coming from the different modeling of the flux function.

The numerical results show that both WENO-SW and WENO-GKS yield quantitatively similar solutions and agree with each other when a sufficient number of mesh points is used to resolve the flow structure. However, with the reduction of mesh points, the WENO-GKS appears to have less numerical dissipation than the WENO-SW, and it gives more accurate solutions in all cases. For the Navier-Stokes solution, the WENO-GKS couples inviscid and viscous terms in a single flux evaluation from an initial WENO reconstruction. However, the WENO-SW, like many other shock capturing schemes, uses operator splitting approach to discretize the inviscid and viscous terms. Due to the different stencil used for the inviscid and viscous terms, in the cavity flow simulation, it shows that the solution of the WENO-SW is more sensitive to the boundary treatment or the reconstruction scheme. With a coarse mesh, the cavity simulation clearly shows the superiority of the WENO-GKS in the capturing of flow structures in comparison with the WENO-SW. Even with 3 mesh points in the boundary layer, the WENO-GKS seems present an accurate viscous solution. Also, the WENO-SW has difficulty in obtaining steady state solution. For the flow interaction from the coupled effect of transport, inviscid, viscous and heat conducting terms, the use of an operator-splitting approach in a high-order scheme is problematic, especially in the barely resolved flow region. In summary, the WENO-GKS is more robust and accurate than WENO-SW, but it is more expensive. Due to its smooth transition from the upwind to the central difference in its flux construction, the WENO-GKS is not sensitive to the reconstructed initial discontinuities, because the whole reconstructed curve inside each cell will participate in the gas evolution around a cell interface. It is noted that more accurate numerical solutions can be obtained from GKS with the use of a large time step, i.e., a large domain will effect the flux, because the whole curve inside each cell is more reliable than point-wise values at the cell interface. In conclusion, besides high-order reconstruction, a high-order gas evolution model is important in the construction of high-order schemes.

Acknowledgments

We would like to thank J.C. Huang and Y.X. Ren for helpful discussion about high-order schemes, especially about the accurate simulation of cavity flow using WENO-type schemes. This work was supported by Hong Kong Research Grant Council (621709, 621011) and National Natural Science Foundation of China (Project No. 10928205).

References

[1] M. Ben-Artzi, J. Li and G. Warnecke, A direct Eulerian GRP scheme for compressible fluid flows, J. Comput. Phys., 218 (2006), pp. 19-43.

[2] P.L. Bhatnagar, E.P. Gross, and M. Krook, A Model for Collision Processes in Gases I: Small Amplitude Processes in Charged and Neutral One-Component Systems, Phys. Rev., 94 (1954), pp. 511-525.
[3] J. Casper, Finite-volume implementation of high-order essentially non-oscillatory schemes in two dimensions, AIAA Journal, 30 (1992), pp. 2829-2835.
[4] X.G. Deng, M.L. Mao, G.H. Tu, H.X. Zhang and Y.F. Zhang, High-order and high accurate CFD methods and their applications for complex grid problems, Commun. Comput. Phys., 11 (2012), pp. 1081-1102.
[5] U Ghia, K.N Ghia, C.T Shin, High-Re solutions for incompressible flow using the Navier-Stokes equations and a multigrid method, J. Comput. Phys., 48 (1982), pp. 387-411.
[6] Z.L. Guo, H.W. Liu, L.S. Luo, and K. Xu, A comparative study of the LBM and GKS methods for 2D near incompressible flows, J. Comput. Phys. 227 (2008), pp. 4955-4976.
[7] A. Harten, B. Engquist, S. Osher, S. Chakravarthy, Uniformly high order Essentially Non-Oscillatory schemes III, J. Comput. Phys. 71 (1987) 231C303.
[8] J.C. Huang, H. Linb, J.Y. Yang, Implicit preconditioned WENO scheme for steady viscous flow computation, J. Comput. Phys., 228 (2009), pp. 420-438.
[9] J.C. Huang, K. Xu and P.B. Yu, A unified gas-kinetic scheme for continuum and rarefied flows II: multi-dimensional cases., Commun. Comput. Phys., 12 (2012), pp. 662-690.
[10] G.S. Jiang, C.W. Shu, Efficient implementation of Weighted ENO schemes, J. Comput. Phys. 126 (1996) 202C228.
[11] J.Q. Li, Q.B. Li, K. Xu, Comparison of the Generalized Riemann Solver and the Gas-Kinetic Scheme for Inviscid Compressible Flow Simulations, J. Comput. Phys., 230 (2011), pp. 5080-5099.
[12] Q.B. Li, K. Xu, and S. Fu, A high-order gas-kinetic Navier-Stokes solver, J. Comput. Phys., 229 (2010), pp. 6715-6731.
[13] W. Li, Y.X. Ren, High-order k-exact WENO finite volume schemes for solving gas dynamic Euler equations on unstructured grids, Int. J. Numer. Meth. Fluids, (2011).
[14] X.D. Liu, S. Osher, Weighted essentially non-oscillatory schemes, J. Comput. Phys., 115 (1994), pp. 200-212.
[15] J. Luo, K. Xu, A high-order WENO-gas-kinetic scheme for hydrodynamic equations, preprint (2012).
[16] T. Ohwada and S. Fukata, Simple derivation of high-resolution schemes for compressible flows by kinetic approach, *J. Comput. Phys.* **211** (2006), pp. 424.
[17] J.M. Qiu and C.W. Shu, Conservative semi-Lagrangian finite difference WENO formulations with applications to the Vlasov equation, Commun. Comput. Phys., 10 (2011), pp. 979-1000.
[18] Y.X. Ren, M. Liu, H.X. Zhang, A characteristic-wise hybrid compact-WENO scheme for solving hyperbolic conservation laws, J. Comput. Phys., 192 (2003), pp. 365-386.
[19] Y.Q. Shen, G.C. Zha,Low diffusion E-CUSP scheme with implicit high order WENO scheme for preconditioned Navier-Stokes equations, Comput Fluids, 50(2012), pp. 13-23.
[20] C.W. Shu, Essentially non-oscillatory and weighted essentially non-oscillatory schemes for hyperbolic conservation laws, Lecture Notes in Mathematics, Springer, 1998.
[21] C.W. Shu, High-order finite difference and finite volume WENO schemes and discontinuous Galerkin methods for CFD, International Journal of Computational Fluid Dynamics, 17 (2003), pp. 107-118.
[22] C.W. Shu and S. Osher, Efficient implementation of essentially nonoscillatory shock-capturing schemes II, J. Comput. Phys., 83 (1989), pp. 32-78.
[23] J.L. Steger and R. Warming,Flux vector splitting of the inviscid gas dynamic equation with

application to finite difference methods, J Compt. Phys, 40(1981), pp. 263- 293.
[24] M.D. Su, K. Xu, M. Ghidaoui, Low Speed Flow Simulation by the Gas-kinetic Scheme, J. Comput. Phys., 150 (1999), pp. 17-39.
[25] P. Woodward and P. Colella, Numerical simulations of two-dimensional fluid flow with strong shocks, J. Comput. Phys., 54 (1984), pp. 115-173.
[26] K. Xu, A gas-kinetic BGK scheme for the Navier-Stokes equations and its connection with artificial dissipation and Godunov method, J. Comput. Phys., 171 (2001), pp. 289-335.
[27] K. Xu and X.Y. He, Lattice Boltzmann method and Gas-kinetic BGK scheme in the low Mach number viscous flow simulations, J. Comput. Phys. 190 (2003), pp. 100-117.
[28] K. Xu and J.C. Huang, A unified gas-kinetic scheme for continuum and rarefied flows, J. Comput. Phys. 229 (2010), pp. 7747-7764.
[29] K. Xu and E. Josyula, Continuum formulation for non-equilibrium shock structure calculation, Commun.Comput. Phys. 1 (2006), pp. 425-448.